

Generation of low-symmetry perovskite structures for *ab initio* computation

N. Xie,¹ J. Zhang,¹ N. Zhang,² X. Chen,^{3,4} and D. Wang^{1,*}

¹*School of Microelectronics & State Key Laboratory for Mechanical Behavior of Materials, Xi'an Jiaotong University, Xi'an 710049, China*

²*Electronic Materials Research Laboratory–Key Laboratory of the Ministry of Education and International Center for Dielectric Research, Xi'an Jiaotong University, Xi'an 710049, China*

³*Department of Applied Physics, Aalto University, Espoo 00076, Finland*

⁴*BroadBit Batteries Oy, Espoo 02150, Finland*

(Dated: January 27, 2022)

Ion displacements are the cause of the ferroelectricity in perovskites. By properly shifting ions, *ab initio* computations have been extensively used to investigate properties of perovskites in various structural phases. In addition to the relatively simple ion displacements, perovskites have another type of structural distortion known as antiferrodistortion or oxygen octahedron tilting. The interplay between these two types of distortions have generated abundant structural phases that can be tedious to prepare for *ab initio* computation, especially for large supercells. Here, we design and implement a computer program to facilitate the generation of distorted perovskite structures, which can be readily used for *ab initio* computation to gain further insight into the perovskite of a given structural phase.

I. INTRODUCTION

Perovskites of the general formula ABX_3 had been used in many areas due to their excellent physical properties¹, including dielectric, magnetic, electrical, optical, and catalytic properties that have been widely investigated^{2–4}. Their piezoelectricity and ferroelectricity have been used for ultrasonics, transducers, pressure sensors, infrared thermoelectric detector, and high density information storage for a long time and such applications have gradually matured over time⁵. Recently, it was also found that organic and inorganic (halide) perovskites can be good candidates for solar cells and light emitting devices.⁶ In particular, perovskite solar cells have been intensively investigated in search of greater conversion efficiency in addition to their simple preparation process and low manufacturing cost.^{7–9}

Predicting the stable phases of perovskites (and their stability) remains a challenge in the investigation of related perovskites for photovoltaics and electrocatalysts.^{10,11} All-inorganic perovskite materials [e.g., halide perovskites $CsBX_3$ ($B = Sn$ and Pb ; $X = I$, Br , and Cl)], without any volatile organic components^{12–15}, exhibit superior thermal stability comparing to organic-inorganic composite perovskite materials. However, understanding the stability of their structural phases is also critical.¹⁶ For instance, cubic phase $CsPbI_3$ has a suitable band gap of 1.7 eV for high-efficiency photovoltaics, but it is not a thermodynamically stable phase at room temperature.^{17,18} Thereby, it is desirable to know the structural phase instabilities and be able to predict the most stable phase and their basic properties can be obtained via *ab initio* computation before material synthesis.

Perovskites often exhibit a wide range of structural distortions originating from lattice instabilities of their prototype cubic structure.¹⁹ For instance, while a large number of perovskite ferroelectrics have uniform polar distortions (e.g., in $PbTiO_3$, $BaTiO_3$, $KNbO_3$), others can have more complex phases involving antiferroelectric ion displacements and oxygen octahedron tilting (e.g., in $PbZrO_3$ and in $SrTiO_3$). The solid solution $Pb(Zr_{1-x}Ti_x)O_3$ embodied such complex

ity with its ever changing structural phases with x .^{20–22} Given the infinite possibilities of perovskite compounds, reliably obtaining the most stable structural phase for them is not a trivial work. The oxygen octahedron tilting is particularly difficult to treat and analyze as the amplitudes and energies due to the distortions are rather small.²³

In order to find the most stable phase, one common practice is to calculate the phonon spectra, obtain the eigenvectors of the unstable phonon modes, shift the ions accordingly, and finally relax the constructed structure using *ab initio* computation to obtain its energy.^{24–28} In addition, the effective Hamiltonian approach has also been successful in predicting and suggesting low-energy phases^{20,33,34}. This approach relies on the fact that low-energy phases are often derived by ion displacements with respect to the original cubic cell (with the $Pm\bar{3}m$ space group) and some distortion of the cell shape. With the cubic phase as the reference structure, two sets of parameters, which are (i) the local mode for ion displacements^{20,29,33–36} and (ii) the antiferrodistortive mode for oxygen octahedron tiltings^{23,37–41}, are used to describe the distortion. The effective Hamiltonian approach uses both local mode and local oxygen tilting as the dynamical variables to construct the energy terms, which are the basis for the subsequent Monte-Carlo and molecular dynamics simulations. The basic construct of the effective Hamiltonian is the “local mode” on each lattice site (often denoted by u_i), these local modes on all lattice sites together can simulate the unstable optic phonon branches and reproduce relevant physics²⁹. With the local mode (and later the oxygen octahedron tilting) and properly constructed energy terms, Monte-Carlo or molecular dynamics simulations can predict the low energy structures of a given perovskite^{30,31}. Afterward, first principles calculations³² can be employed to verify if a proposed structure is indeed the ground state by comparing it to other structural phases. The comparison here requires the construction of various crystal phases for *ab initio* computation.

In constructing various structural phases, ion displacement is easy to understand and keep track of. For instance, while $BaTiO_3$ has a complex sequence of ferroelectric phase transitions, the resulting tetragonal, orthorhombic, rhombohedral,

ferroelectric phases can all be understood in terms of the Ti ions shifting along different directions. On the other hand, the second type of distortion (which could also be part of the overall phase transition) involves small tiltings or rotations of the BX_6 octahedra (usually the oxygen octahedra), which is more difficult to deal with due to the corner sharing of the X on neighboring sites that constrains possible movements.^{42–44} For instance, the TiO_6 octahedra in SrTiO_3 are not independent of each other and can only exhibit certain patterns. One possibility is that the TiO_6 s rotate about the **c**-axis with neighboring octahedra rotate in opposite directions. Some perovskites (e.g., CaTiO_3) can demonstrate even more complex rotation patterns and it was M. Glazer who first proposed a systematic notation to describe such patterns^{37,38}, now commonly known as the Glazer notation.

In order to facilitate the search of stable structural phases with first principles calculations, we design and implement a Python program named `PyTilting` that can systematically generate different structural phases that encompass distortions involving both the local mode and the oxygen tilting. With this tool, it is possible to automate the structure construction process, an essential step in high throughput *ab initio* computation^{45–47}.

II. STRUCTURAL DISTORTIONS

The perovskite structure contains a network of corner-sharing octahedra. Considering such constraints, the following rules apply when we consider tiltings: (i) The axis of the tilting can be parallel to any crystallographic axis, which requires a vector $\boldsymbol{\omega} = (\omega_x, \omega_y, \omega_z)$ to describe it; (ii) The amplitude of each tilting may be different from the others, that is, ω_x , ω_y , and ω_z can be independent of each other; (iii) Two subsequent layers being stacked along the tilting axis may be tilted in-phase or anti-phase. However, neighboring octahedron on the plane perpendicular to the tilting axis has to be in anti-phase.

For a $2 \times 2 \times 2$ supercell with PBC, there are 23 tilting patterns that can derive from the cubic perovskite.^{37,39} However, when the displacement of atoms is involved and combined with these tiltings, the situation becomes quite complicated. It is not trivial in many cases to translate a desired distortion into a structure setup with proper space group and symmetry, which can be readily employed in *ab initio* calculations. To address this challenge, we have designed programs to realize such distortions in terms of ion displacements, obtaining the low-symmetry structures from the cubic high-symmetry structure ($Pm\bar{3}m$). In this section, we will first discuss the general features of octahedron tilting and ion displacement.

A. Octahedron tilting

Glazer notation has become the standard way to describe tilting distortions, concisely summarizing tilting patterns into strings such as $a^0b^+b^+$ and $a^0b^+b^-$. To decipher such strings, we first note that they can be split into three groups,

each describing the tilting situation around one axis, in the order of **a**, **b**, **c**-axes. Each group contains a letter specifying the magnitude of the tilting. The second parameter is a superscript indicating whether the rotations in adjacent layers are in the same or opposite directions (in-phase or out-of-phase rotation). A negative superscript (a^-) indicates that the tiltings of two neighboring octahedra, along the tilting axis, are in the opposite directions, while a positive superscript (a^+) is used when they tilt in the same direction. A zero superscript (a^0) is used when no tilting occurs (see below for more illustration). Given the fact that neighboring octahedron has to tilt/rotate oppositely if the axis of rotation is perpendicular to the line connecting the center of the two oxygen octahedra, each group also provides enough information regarding the tiltings on each unit cell. This fact is implicitly used in our program.

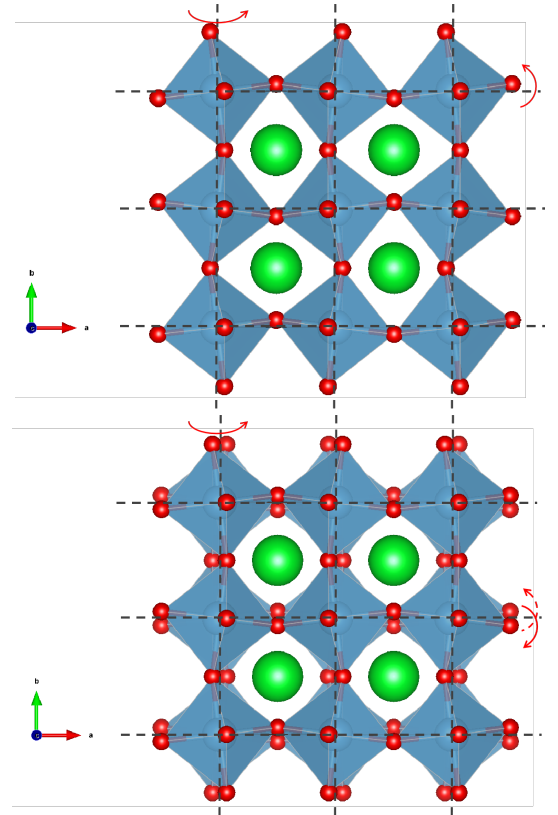


FIG. 1. The projection of SrTiO_3 along the **c**-axis: (a) $a^0b^+b^+$ and (b) $a^0b^+b^-$ rotation patterns. The blue, red, and green balls represent Ti, O, and Sr atoms, respectively. The gray grid line provides a reference position for the Ti-O bond. The offset of the oxygen atoms from the vertical grid lines indicates that the octahedron rotates in the same direction around the **b**-axis, while the zero offset from the horizontal grid lines indicates that the oxygen octahedron does not rotate around the **a**-axis. In Figure (a), the upper and lower oxygen octahedra (along the **c**-axis) rotate in the same direction around the **c**-axis, while in (b) they rotate in the opposite direction.

To illustrate the Glazer notation, we show the tilting patterns $a^0b^+b^+$ and $a^0b^+b^-$ in Fig. 1. Clearly, these two Glazer notation specifies no tilting around the **a**-axis, but tilt-

ings around the **b**-axis and **c**-axis. In addition, for both cases, counting along the **b**-axis, neighboring unit cells have the same (in-phase) tiltings around the **b**-axis, but counting along the **c**-axis, neighboring unit cells have the opposite (out-of-phase) tiltings around the **c**-axis.

As we can see, it takes some effort to decipher the tilting patterns specified by the Glazer notation. To reduce this unnecessary work, our program fully understands the exact meaning of Glazer notation, can decode them, and construct the desired structure for an arbitrary (but properly chosen) supercells. For instance, it can easily reproduce the 23 simple tilting systems with a $2 \times 2 \times 2$ supercell, generating all the cases in which the oxygen octahedra have rotations on one, two, or three axes. Large supercells with more exotic tilting patterns can also be specified with minimal additional programming.

B. Ion displacement

Having considered tilting, we now consider ion displacement, which is easier because, unlike tilting, ion displacements on each unit cell can be independently specified by three numbers $\mathbf{u} = (u_x, u_y, u_z)$ on each unit cell where u_x , u_y , and u_z are the magnitudes of ion shifting along the **a**-, **b**-, and **c**-axis. With the information of the local mode, which specifies how the ions inside each unit cell relatively shifts, the ion displacements can all be specified throughout the system.

To be compatible with the periodic boundary condition, patterns of the local mode over the $2 \times 2 \times 2$ supercell can be specified by using the high-symmetry points inside the Brillouin zone: $\Gamma = (0, 0, 0)$, $X = (1, 0, 0)$, $M = (1, 1, 0)$, and $R = (1, 1, 1)$ (or other points with larger supercells). For instance, the Γ point specifies a uniform \mathbf{u} over the whole supercell. We note that the local mode patterns for u_x , u_y , u_z can be specified independently. Practically, the local mode can be determined from phonon eigenvectors (or eigenvectors of the force constant matrix)³⁴. Here, for convenience, we usually just displace the B atom to achieve the desired low-symmetry structure. Employing more complex local mode is often inconsequential since the resulting structure will be further relaxed by *ab initio* softwares, most of which can be set to respect the starting symmetry of a given system.

III. IMPLEMENTATION

With the above discussion in mind, we design a program *pyTilting* to automatically generate the low-symmetry structures involving distortions of both tilting and displacement. The program is designed to export to ASE atoms object⁴⁸ or a cif files, which can be used in other *ab initio* softwares, or directly integrated with the specific software (e.g., GPAW⁵⁹). Furthermore, it is easily to download all the program and obtain related documentation online⁶⁰. While our implementation can build an arbitrary supercell, we will focus on the $2 \times 2 \times 2$ supercell that can represent most interesting structures. In particular, the 23 structures with only tilting can be

represented with such a supercell.

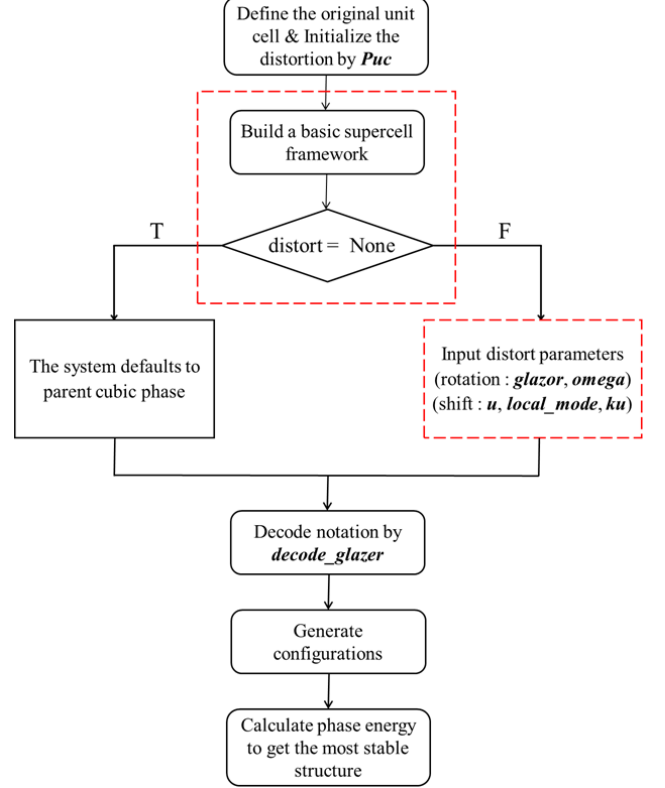


FIG. 2. The execution flow of the program.

Figure 2 shows the flow of the program. It comprises several steps from top to bottom: (i) First, the initial configuration is defined with the most basic parameters (e.g, atomic symbols), setting the ions to their ideal cubic positions. All atoms can shift but only oxygen atoms are allowed to rotate. A Python class `Puc` is defined for this task; (ii) Next, the unit cell information is inherited by the class `Distortion`, which builds a supercell by repeating the unit cell according to the grid and `lattice_constant` parameter; (iii) In the next step, the program determines the structural distortion given by the user. If no distortion is desired, the system defaults to the parent phase ($Pm\bar{3}m$), otherwise the user's input regarding the distortion is read; (iv) The Glazer notation is decoded by the function class `decode_glazer`. (v) Generating the desired structures with the information regarding distortion; (vi) Finally, the generated structures can be used in other *ab initio* calculations. The red boxes in Fig. 2 indicate the necessary inputs to characterize the distortions. The program and the inputs are explained below.

A. Unit cell and supecell

The program defines a Python class `Puc` that contains information of perovskite primitive unit cell (PUC, each containing 5 atoms) and basic operations, such as the `shift` and `rotate` functions that operate on the PUC level. At

initialization, the default atom symbols are set to be “A”, “B” and “O” referring to ABO_3 , but custom atom symbols can also be set. The five atoms in each PUC are initially placed at their ideal positions with fractional coordinates, $\mathbf{p}_A = [0.5, 0.5, 0.5]$, $\mathbf{p}_B = [0.0, 0.0, 0.0]$, $\mathbf{p}_{O_1} = [0.5, 0.0, 0.0]$, $\mathbf{p}_{O_2} = [0.0, 0.5, 0.0]$, $\mathbf{p}_{O_3} = [0.0, 0.0, 0.5]$.

Only oxygen atoms are allowed to rotate in the `rotate` function. The new coordinates after rotation are obtained with $\mathbf{p} = c_0(\boldsymbol{\omega} \times \mathbf{p}_0) + \mathbf{p}_0$, where $\boldsymbol{\omega}$ is the vector of angle that describes the tilting, \mathbf{p}_0 is the initial position of the oxygen atom, and c_0 is a list represents the c/a ratio of the \mathbf{c} -axis lattice constant divided by the \mathbf{a} -axis lattice constant (defaults to 1). In the `shift` function, the coordinates of all atoms can be updated according to the formula $\mathbf{p} = \Delta\mathbf{p} + \mathbf{p}_0$ where the displacement $\Delta\mathbf{p}$ is calculated according to the local mode vectors and other input regarding dipole patterns.

After setting up the PUC, the `Distortion` class build a supercell encompassing many identical PUCs and setup the distortion on the supercell level, accommodating possible structural phases. The parameter `grid=(n_x, n_y, n_z)` specifies how many unit cells repeat along the \mathbf{a} -, \mathbf{b} -, and \mathbf{c} -axis.

The program includes some basic constructs consisting of several basic parameters: (i) The atom symbols for ABX_3 ; (ii) The lattice constant; (iii) The `grid` parameter for supercell; and (iv) The c/a ratio. Other parameters specifying the actual distortions and their use are discussed below.

B. Specifying distortions

Based the two distortion mechanisms discussed in Sec. II, tilting and ion displacement need to be specified as input for the program.

1. Decoding Glazer notation

```
def decode_glazer(s):
    if(len(s) != 6):
        print("glazer notation has the form 'a-a-a-',
              your input seems incorrect.")
        exit()
    k_ox = [1,1,1]
    if (s[1] == '-'):
        k_ox = [1,1,1]
    elif (s[1] == '+'):
        k_ox = [0,1,1]
    elif (s[1] == '0'):
        k_ox = [0,0,0]
    else:
        print("glazer notation has the form 'a-a-a-',
              your input seems incorrect.")
        exit()
```

FIG. 3. Decoding Glazer notation.

For tilting, the program needs to properly change the positions of oxygen atoms. Since the Glazer notation is the stan-

dard way to describe the tilting in a perovskite system, it is natural to use it as the input for the program and thus their meaning needs to be properly decoded in the program.

In a Glazer notation, the superscript 0, +, or - corresponds to no tilting, in-phase, and out-of-phase tilting of neighboring oxygen atoms, respectively. Such tilting patterns corresponds to high-symmetry points in the Brillouin zone that are Γ ($\mathbf{k} = [0, 0, 0]$), M ($\mathbf{k} = [0, 1, 1]$) and R ($\mathbf{k} = [1, 1, 1]$). Due to the constraint of the corner sharing of octahedra, the superscript determines which point to choose. Let us use the tilting around the \mathbf{a} -axis as an example (i.e., ω_x in the first group of a Glazer notation): (i) The superscript - means $\mathbf{k}_{\omega_x} = [1, 1, 1]$ (R), i.e., ω_x changes its sign whenever it moves to the next nearest neighbor; (ii) The superscript + means $\mathbf{k}_{\omega_x} = [1, 1, 1]$, i.e., ω_x changes its sign whenever it moves to the next first nearest neighbor along y or z , but keep the same sign when it moves along x ; (iii) The superscript 0 means $\mathbf{k}_{\omega_x} = [0, 0, 0]$, i.e., the same tilting on all sites, which in fact forces $\omega_x = 0$. Similarly, the other two groups specifies how ω_y and ω_z are arranged over the whole crystal.

The actual implementation to decode Glazer notation is shown in Fig. 3. Combining \mathbf{k}_{ω_x} , \mathbf{k}_{ω_y} , and \mathbf{k}_{ω_z} , we know how the octahedron tilts in each unit cell. After determining the arrangements of $\omega_{x,y,z}$, the program also checks if the input tilting angles are consistent with the arrangement, and if ω_x , ω_y and ω_z shall be equal to each other. For instance, the notation $a^+a^+c^+$, means $\omega_x = \omega_y \neq \omega_z$. If inconsistency is encountered, the program will print warnings and stop execution.

2. Displacement

```
def shift(self, u=[0,0,0],
          local_mode=[[0.0,0.0,0.0,0.0,0.0]]):
    dA=local_mode[0]
    dB=local_mode[1]
    dOp=local_mode[2]
    dOq=local_mode[4]
    dpq = np.array([
        [dA, dA, dA],
        [dB, dB, dB],
        [dOp, dOp, dOp],
        [dOp, dOq, dOp],
        [dOp, dOp, dOq]
    ])
    du = np.array([
        [u[0], 0., 0.],
        [0., u[1], 0.],
        [0., 0., u[2]]
    ])
    rslt = np.matmul(dpq, du)
    for i in range(5):
        self.atoms[i]['pos'] += rslt[i]
```

FIG. 4. Mathematical representation of the displacement.

Two matrices are used to characterize ion displacements. The eigenvector of the local mode (soft mode) in perovskites

can be characterized by four parameters: d_A (ξ_A), d_B (ξ_B), d_{O_p} (ξ_{O_\perp}) and d_{O_q} (ξ_{O_\parallel})³⁴, which corresponds to displacements of the A atom, B atom, the O atom forming the B-O bond along the displacement direction, and the other two O atoms forming the B-O bonds perpendicular to the displacement direction, respectively. Considering the fact that the x , y , and z directions are equivalent (for the cubic phase used as the reference structure), the displacements can be mathematically represented by a 5×3 matrix dpq as shown in Fig. 4. The amplitude of the local mode is denoted by $\mathbf{u} = (u_x, u_y, u_z)$, which contains displacements along x (u_x), y (u_y), and z (u_z) directions represented by a 3×3 diagonal matrix du . The actual displacement for each atom can be realized by the matrix product of dpq and du as shown in Fig. 4.

Similar to setting the patterns for tilting, we also need to set the \mathbf{k} vectors to specify how local mode du changes from one unit cell to the next. With k_{u_x} , k_{u_y} , and k_{u_z} being independent of each other, for a $2 \times 2 \times 2$ supercell, k_{u_x} , k_{u_y} , and k_{u_z} can be chosen from $\Gamma = (0,0,0)$, $X = (1,0,0)$, $M = (1,1,0)$, or $R = (1,1,1)$.

C. Example input

To illustrate the use of the program, we show how to construct certain structures of bismuth ferrite (BiFeO_3) step by step. It is known that BiFeO_3 can have ferroelectric ($R3c$) and antiferroelectric phases ($Pnma$) that, combined with its magnetic properties, make it a popular multiferroic material.^{49–52} The $R3c$ phase (space group: #161) can be thought of as stretching the ideal cubic structure in the $[111]$ direction, which is made more complex by the $a^-a^-a^-$ tilting, resulting in a rhombohedral phase.^{51,52}

```
s = Distortion(
    system={
        'symbols': ['Bi', 'Fe', 'O'],
        'lattice_constant': 3.96,
        'grid': (2, 2, 2),
        'covera': 1.0
    }
)
```

FIG. 5. Program input to setup basic properties of the material BiFeO_3 .

The program first needs the lattice constant and atom symbols to identify the material to be calculated. We set the lattice constant of BiFeO_3 3.96 Å, with a $2 \times 2 \times 2$ supercell (grid). The parameter *covera* (c/a) accounts for the possible lattice stretch along the c axis, which can be convenient sometimes but not always necessary (c/a defaults to 1.0). The setup at this stage is shown in Fig. 5.

In the second stage, with the Glazer notation for BiFeO_3 's $R3c$ phase being $a^-a^-a^-$ (glazer), we enter the tilting angle $\omega = (0.1, 0.1, 0.1)$ in radian, which is just an estimate of the magnitude of tilting and completes setup for the tilting distortion as shown in Fig. 5. We also need to endow a small displacement by input the magnitude (u) and vector

```
def test_R3c(self):
    s.distort = {
        'glazer': 'a-a-a-',
        'omega': (0.1, 0.1, 0.1),
        'u': (0.1, 0.1, 0.1),
        'k_u': [[0, 0, 0], [0, 0, 0], [0, 0, 0]],
        'local_mode': [0.00, 0.50, 0.00, 0.00, 0.00],
    }
    atoms = s.get_atoms()
    atoms.write('./a-a-a-.cif')

    sg = my_get_spacegroup(atoms, method = 'spglib')
    print(sg.no)
    self.assertEqual(sg.no, 161)
```

FIG. 6. Program input to setup the distortion for the $R3c$ phase of BiFeO_3 .

(local_mode) of the local modes. Assuming the amplitude of the local mode is given by $\mathbf{u} = (u_x, u_y, u_z)$ as mentioned in the Sec. II B, the program automatically calculates and actuates the displacement for each ion in a unit cell as shown in Fig. 4. Meanwhile, the wave vector for the local mode is input as a matrix k_u with the rows representing k_{u_x} , k_{u_y} , and k_{u_z} . Knowing that the $R3c$ phase has polarization along the (111) direction, we set $\mathbf{u} = (0.1, 0.1, 0.1)$ and the wave vector at the Γ point ($\mathbf{k} = [0, 0, 0]$) as shown in Fig. 4.

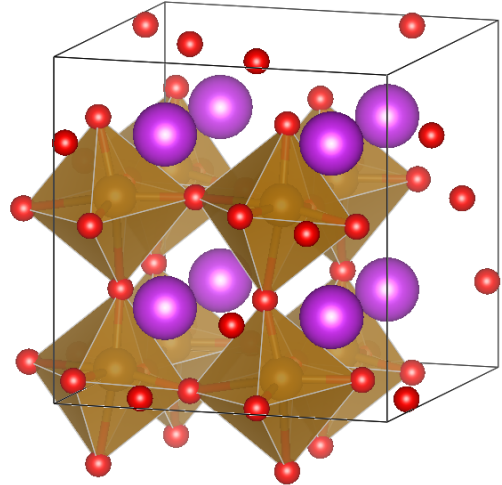


FIG. 7. The generated $R3c$ phase of BiFeO_3 .

Finally, we generate the atoms object that can be used directly by ASE, GPAW, or exported to *cif* file. The symmetry of the generated structure (see Fig. 7) can be checked by ASE as shown in Fig. 7.

IV. APPLICATION

In this section, we apply the program to identify the most stable phase of a halide perovskite, that is CsSnI_3 . Halide per-

ovskite has attracted much attention for their use in solar cells for their high energy conversion efficiency and tunable band gaps.^{53,54} CsSnI₃ is an unusual perovskite that undergoes a series of complex phase transitions and exhibits near-infrared emission at room temperature. The phase-stabilized CsSnI₃ is important for its application in the photovoltaic and optoelectronic fields^{53,55,56}.

A. Phonon analysis

In order to reduce the number of possible structural phases, we perform a screening to eliminate certain phases in order to save time and computing resource by calculating the phonon band structure and perform some initial analysis that focuses on the unstable modes. For instance, negative (or imaginary) frequencies at the Γ point are associated with uniform global displacement of ions, which often implies ferroelectricity.

For ion displacement, in addition to the Γ point, other points from the Brillouin zone can also be used to specify the dipole patterns (possible choices are constrained by the size of the supercell). On the other hand, only two points are important for tilting, which are (i) the M point, $\mathbf{q} = (1/2, 1/2, 0)$ and (ii) the R point, $\mathbf{q} = (1/2, 1/2, 1/2)$.

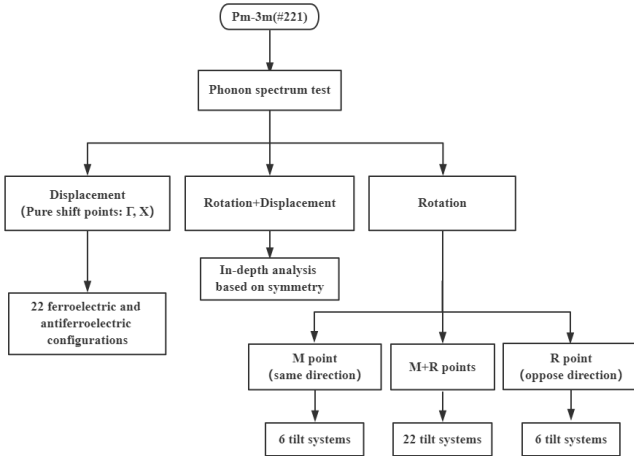


FIG. 8. Combining phonon spectra to analyze phase transitions.

The above analysis can be summarized into the flow chart in Fig. 8, where we assume the M and R point are only related to tilting and the Γ and X point are related to displacements. The possibility that M and R points accommodates antiferroelectric phases requires additional analysis of the phonon eigenvectors at these two points.

If the phonon spectrum only has a virtual frequency at the Γ , the stable phase is most likely ferroelectric, as well as the X point, other antiferroelectric phases also need to be considered – there are 22 high-symmetry configurations for pure-shift points containing 14 with $u_x = u_y = u_z \neq 0$, 6 with $u_\alpha = u_\beta \neq 0$, and 2 with $u_\alpha \neq 0$, where $\alpha, \beta = x, y, z$.

For pure tilting, there are three scenarios: (i) The virtual frequency only appears at the M point, resulting in 6 cases (out of 23) need to be considered; (ii) The virtual frequency

only appears at point R , then again resulting in 6 cases (out of 23) need to be considered; (iii) If both the M and R points have virtual frequencies, all 23 tilting patterns need to be considered. The most complicated scenario occurs when all the high symmetry points have virtual frequencies, resulting in the superposition of tilting and displacement that requires further analysis.

B. Results

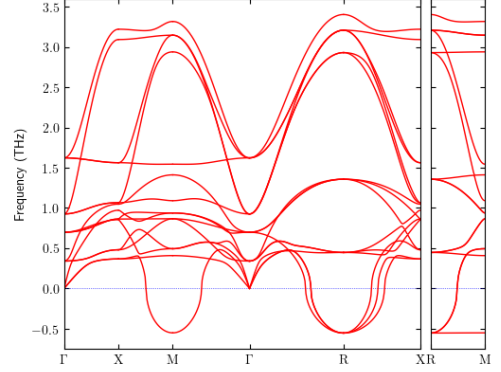


FIG. 9. The phonon spectrum of CsSnI₃

The phonon calculation for CsSnI₃ was done using Phonopy⁶⁵ with GPAW. To get accurate results, we have used $2 \times 2 \times 2$ supercell in the phonon calculation, which agree with Ref.⁶⁷ very well. The phonon spectrum shown in Fig. 9 clearly demonstrates that CsSnI₃ has the strongest instabilities at the M and R points, which involve all the tilting patterns. On the other hand, there is no instability at the Γ or X point, which eliminates many possible structural phases.

To find the most stable structural phase, we use the program to generate all the 23 tilting patterns for *ab initio* calculation using the projector augmented plane wave (PAW) method as implemented in the GPAW Package^{58,59} with the Perdew–Burke–Ernzerhof (PBE) functional⁵⁷. A $4 \times 4 \times 2$ Monkhorst-Pack⁶³ sampling is used for the k -space integration. The valence orbitals used in the first-principles calculations are: Cs ($5s\ 6s\ 5p$), Sn ($5s\ 5p\ 4d$) and I ($5s\ 5p$). The structures are relaxed with a plane-wave cutoff of 900 eV until atomic forces fall below 0.05 eV/Å. As shown in Figure 7, it is clear that the highest energy belongs to the parent phase of $Pm\bar{3}m$, while the phase with the lowest energy has the tilting $a^+b^-b^-$.

Table I shows all the 23 tilting patterns for CsSnI₃ with its Glazer notation and symmetry group. We note the results are consistent with the tilting system proposed by Glazer, except for the tilting systems No. 5 ($a^+b^+b^-$) and No.7 ($a^+a^+a^-$). These two systems should have the $P42/nmc$ phase (space group: 137) instead of the $Pmmm$ phase (space group: 59) that was initially proposed³⁷, which has been confirmed by other

Number	Tilting	Symmetry	Energy(meV)
3 tilts			
1	$a^+b^+c^+$	$Immm$ (#71)	-83.7
2	$a^+b^+b^+$	$Immm$ (#71)	-83.0
3	$a^+a^+a^+$	$Im\bar{3}$ (#204)	-82.5
4	$a^+b^+c^-$	$Pmmn$ (#59)	-130.2
5	$a^+a^+c^-$	$P4_2/nmc$ (#137)	-118.6
6	$a^+b^+b^-$	$Pmmn$ (#59)	-124.9
7	$a^+a^+a^-$	$P4_2/nmc$ (#137)	-118.9
8	$a^+b^-c^-$	$P2_1/m$ (#11)	-150.4
9	$a^+a^-c^-$	$P2_1/m$ (#11)	-144.2
10	$a^+b^-b^-$	$Pnma$ (#62)	-151.2
11	$a^+a^-a^-$	$Pnma$ (#62)	-148.8
12	$a^-b^-c^-$	$P\bar{1}$ (#2)	-97.8
13	$a^-b^-b^-$	$C2/c$ (#15)	-92.6
14	$a^-a^-a^-$	$R\bar{3}c$ (#167)	-91.4
2 tilts			
15	$a^0b^+c^+$	$Immm$ (#71)	-91.6
16	$a^0b^+b^+$	$I4/mmm$ (#139)	-88.8
17	$a^0b^+c^-$	$Cmcm$ (#63)	-124.6
18	$a^0b^+b^-$	$Cmcm$ (#63)	-122.1
19	$a^0b^-c^-$	$C2/m$ (#12)	-103.9
20	$a^0b^-b^-$	$Imma$ (#74)	-100.8
1 tilt			
21	$a^0a^0c^+$	$P4/mbm$ (#127)	-82.9
22	$a^0a^0c^-$	$I4/mcm$ (#140)	-83.9
no tilt			
23	$a^0a^0a^0$	$Pm\bar{3}m$ (#221)	0.0

TABLE I. 23 tilting systems for CsSnI₃ and their energies (the energy of the $Pm\bar{3}m$ phase is used as the reference energy).

literature.^{23,39,41,66}

The energy of the four systems No.8 to No.11 is quite close to each other, with a difference of ~2.5 meV. Coincidentally, this phenomenon also appears for No.1 to No.3, and their energy difference is as small as ~1 meV, and No. 8 and No. 10 with difference less than 1 meV. It is also worth mentioning that even if some configurations have the same space group, their tilting patterns are still different (see No.1, 2 and 15 in Tab. I), resulting in different energies.

V. DISCUSSION

A. CsSnI₃

The space groups and the most stable structure predicted here agree well with experimental results and other theoretical or computational results^{53–56,67}. For CsSnI₃ crystal (black phase), it is known to undergo a number of successive phase transitions as a function of temperature, corresponding to rota-

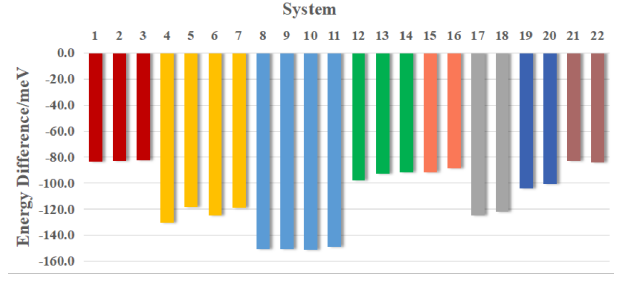


FIG. 10. The energy of the 22 tilting configurations after geometry relaxation.

tions and rearrangements of the SnI₆ octahedron. The cubic phase (B- α) is only stable at high temperature, which turns into the tetragonal $P4/mbm$ phase at 380 K (B- β), then to the orthorhombic $Pnma$ at 300 K (B- γ).

The tolerance factor t is a powerful predictor to tilting distortions. It turns out that the case size for the Cs atom in the ideal cubic phase, which is set by the Sn-I octahedron size, is slightly too large. By the definition given by Benedek and Fennie⁶⁸, $t = R_{AC}/\sqrt{2}R_{BC}$ with R_{AC} and R_{BC} being the ideal bond lengths. Using the ideal bond lengths based on Shannon ionic radii⁶⁹, we find $t = 0.90$ for CsSnI₃, indicating that tilting can suppress ferroelectricity, consistent with the general trend of adopting the $Pnma$ phase with $t < 1$. The driving force for this stabilization is to optimize the environment for the A cation (Cs atom here).⁶⁷ Moreover, the $\alpha \rightarrow \beta$ phase transition corresponds to the Glazer tilting $a^0a^0c^+$, and the γ phase is characterized by both octahedral twists about the c axis and tilts about the tetragonal a axis, which refers to the Glazer notation $a^+b^-b^-$. Our results confirm the stability of the $Pnma$ being the most stable phase.

B. Tilting

Our results indicate that the tilting patterns can be divided into several groups, reflecting their geometry features: (1) $a^+b^+c^+$ (No.1~3); (2) $a^+b^+c^-$ (No.4~7); (3) $a^+b^-c^-$ (No.8~11); (4) $a^-b^-c^-$ (No.12~14); (5) $a^0b^+c^+$ (No.15, 16); (6) $a^0b^+c^-$ (No.17, 18); (7) $a^0b^-c^-$ (No.19, 20); (8) $a^0a^0c^+$ (system No.21) and (9) $a^0a^0c^-$ (system No.22). The tilting patterns of the same group tend to have extremely close energy, as demonstrated in Fig. 10 because their mutual conversion only requires a certain adjustment of the tilting angle rather than a change of the tilting pattern, while such adjustment can be actuated in *ab initio* calculations. For instance, $a^+b^-c^-$ could become very close to $a^+b^-b^-$, $a^0b^+c^+$ is similar to $a^0b^+b^+$. This is likely because, after relaxation, the tilting angles become more similar to each other, moving towards the high-symmetry configurations.

According to our results, in each group, if two (or three) axes have the same tilting angle, then higher symmetry is achieved, but resulting in increased energies. In addition, the R -point-related tilting patterns seem to have lower energy than M -point-related tilting patterns when other factors being equal

(e.g. system No.1 and 12, No.2 and 10, No.21 and 22). The calculation of the 23 tilt systems shows that the energy of the structure depends mainly on tilting patterns, not the actual tilting angles.

Finally, it should be mentioned that, for some tilting patterns, small distortions (in addition to tilting) of the octahedra must occur to preserve the connectivity of the octahedra. Such a requirement results in symmetries (and space groups) that are different from expectations purely from the consideration of tilting. For instance, the four tilting patterns in group 2 (No. 4-7) was initially proposed to produce an orthogonal phase (with the space group of 59)³⁷. However, later research^{23,39,41,66} examined the geometrical constraints and found that two of them have the $P4_2/nmc$ symmetry, requiring extra distortion to the octahedra. In other words, such tilting patterns cannot be accommodated without changing the B–O bond lengths. Due to this type of additional distortion, tilting patterns No.5 and 7 are able to form a more symmetrical tetragonal phase, and resulting in higher energies than No.4 and 6, respectively.

VI. SUMMARY

In this work, we have developed a program to generate various tilting patterns for perovskites with the ability to set up ion displacements as well. This program can generate desired configurations for arbitrary superlattices, which is useful to deal with complex structural phases or complex perovskites made by doping or solid solution.

The program adopts two strategies to deal with two major distortions with perovskites: (1) For the tilting, we derive 23 tilting patterns based on the Glazer notation; (2) Use local-mode-based displacements to form polar phases. Combining

these two strategies enables us to generate hybrid structural phases made of both tilting and ion displacement.

To test the program, we have taken CsSnI_3 as an example and use the program to find its most stable structural phase. The strategy is to first obtain the phonon spectrum in order to reduce the number of different phases to examine. With the aid of our software package, the 23 tilting systems are built and their energies calculated. It is found that the $Pnma$ is the most stable phase, corresponding to the $a^+b^-b^-$ tilting with its energy reduced by ~ 150 meV from the cubic $Pm\bar{3}m$ phase.

The computer program is written in Python, which can directly generate configuration files, or easily be integrated into other software packages for first-principles calculations. It is open source online currently and able to download and use. Since our program can build arbitrary supercells, doping effects on a given structure can be dealt with by replacing certain ions in the system after the desired structural phases are generated. With such a tool available, we can build a vast number of different structural phases, the next step will be finding effective ways to screen those candidates quickly so that first-principles computations will be able to quickly provide us the most stable phase of a given perovskite.

ACKNOWLEDGMENTS

This work is financially supported by the National Natural Science Foundation of China, Grant No. 11574246, U1537210, and 11974268. X.C. Thanks the financial support from Academy of Finland Projects 308647 and European Union's Horizon2020, Grant No. 760930. X.C. and D.W. thank the support from CSC (IT Center for Science, Finland), project 2001447, for providing computation resource. D.W. also thanks the support from the Chinese Scholarship Council (201706285020).

* dawei.wang@xjtu.edu.cn

¹ M. E. Lines, and A. M. Glass, *Principles and Applications of Ferroelectrics and Related Materials* (Clarendon Press, Oxford, 1977).

² E.A.R. Assirey, Saudi Pharmaceutical Journal **27** (2019), 817. <https://doi.org/10.1016/j.jsps.2019.05.003>.

³ N. A. Spaldin, and R. Ramesh, Nat. Mater. **18** (2019), 203. <https://doi.org/10.1038/s41563-018-0275-2>

⁴ D. Wang, A. A. Bokov, Z.-G. Ye, J. Hlinka, and L. Bellaiche, Nat. Commun. **7** (2016), 11014. <https://doi.org/10.1038/ncomms11014>

⁵ Z.-G. Ye, Materials Today **11** (2008), 70. [https://doi.org/10.1016/S1369-7021\(08\)70258-X](https://doi.org/10.1016/S1369-7021(08)70258-X)

⁶ L. N. Quan, F. P. García de Arquer, R. P. Sabatini, and E. H. Sargent, Adv. Mater. **30** (2018), 1801996. <https://doi.org/10.1002/adma.201801996>

⁷ N. J. Jeon, J. H. Noh, Y. C. Kim, W. S. Yang, S. Ryu, and S. I. Seok, Nature. **517** (2015), 897. <https://doi.org/10.1038/nature14133>

⁸ H. Chen, F. Ye, W. Tang, J. He, M. Yin, Y. Wang, F. Xie, E. Bi, X. Yang, and M. Grätzel, Nature **550** (2017), 92. <https://doi.org/10.1038/nature23877>

⁹ K. Aitola, K. Domanski, J. P. Correa-Baena, K. Sveinbjornsson, M. Saliba, A. Abate, M. Grätzel, E. Kauppinen, E. M. J. Johansson, W. Tress, A. Hagfeldt, and G. Boschloo, Adv. Mater. **29** (2017), 1606398. <https://doi.org/10.1002/adma.201606398>

¹⁰ S. M. Woodley, and R. Catlow, Nat. Mater. **7** (2008), 937. <https://doi.org/10.1038/nmat2321>

¹¹ C. J. Bartel, C. Sutton, B. R. Goldsmith, et al. Sci. Adv. **5** (2019), eaav0693. <https://doi.org/10.1126/sciadv.aav0693>.

¹² M. Saliba, T. Matsui, K. Domanski, J. Y. Seo, A. Ummadisingu, S. M. Zakeeruddin, J. P. Correa-Baena, W. R. Tress, A. Abate, A. Hagfeldt, and M. Grätzel, Science **354** (2016), 206. <https://doi.org/10.1126/science.aah5557>

¹³ J. Liang, C. X. Wang, Y. R. Wang, Z. R. Xu, Z. P. Lu, Y. Ma, H. F. Zhu, Y. Hu, C. C. Xiao, X. Yi, G. Y. Zhu, H. L. Lv, L. B. Ma, T. Chen, Z. X. Tie, Z. Jin, and J. Liu, J. Am. Chem. Soc. **138** (2016), 15829. <https://doi.org/10.1021/jacs.6b10227>

¹⁴ A. Swarnkar, A. R. Marshall, E. M. Sanhira, B. D. Chernomordik, D. T. Moore, J. A. Christians, T. Chakrabarti, and J. M. Luther, Science **354** (2016), 92. <https://doi.org/10.1126/science.aag2700>

¹⁵ M. Kulbak, S. Gupta, N. Kedem, I. Levine, T. Bendikov, G. Hodes, and D. Cahen, J. Phys. Chem. Lett. **7** (2016), 167.

- <https://doi.org/10.1021/acs.jpcelett.5b02597>
- 16 R. Wang, M. Mujahid, Y. Duan, Z.-K. Wang, J. Xue, and Y. Yang, *Adv. Funct. Mater.* (2019), 1808843. <https://doi.org/10.1002/adfm.201808843>.
 - 17 J. Sun, S. Huang, J. Hu, et al. *J. Am. Chem. Soc.* **140** (2018), 11705. <https://doi.org/10.1021/jacs.8b05949>
 - 18 J. B. Hoffman, A. L. Schleper, and P. V. Kamat, *J. Am. Chem. Soc.* **138** (2016), <https://doi.org/8603.10.1021/jacs.6b04661>
 - 19 M. E. Lines, A. M. Glass, and G. Burns, *Physics Today*, **31** (1978), 56. <https://doi.org/10.1063/1.2995188>
 - 20 U. V. Waghmare, and K. M. Rabe, *Phys. Rev. B* **55** (1997), 6161. <https://doi.org/10.1103/PhysRevB.55.6161>
 - 21 Igor A. Kornev, L. Bellaiche, P.-E. Janolin, B. Dkhil, and E. Suard. *Phys. Rev. Lett.* **97** (2006), 157601. <https://doi.org/10.1103/PhysRevLett.97.157601>
 - 22 N. Zhang, H. Yokota, A. M. Glazer, Z. Ren, D. A. Keen, D. S. Keeble, P. A. Thomas and Z.-G. Ye. *Nat. Commun.* **5** (2014), 5231. <https://doi.org/10.1038/ncomms6231>
 - 23 M. A. Islam, J. M. Rondinelli, and J. E. Spanier, *J. Phys.: Condens. Matter* **25** (2013), 175902 <https://doi.org/10.1088/0953-8984/25/27/275902>
 - 24 M. Mori, and H. Saito, *J. Phys. C: Solid State Phys.* **19** (1986), 2391. <https://doi.org/10.1088/0022-3719/19/14/005>
 - 25 K. Gesi, J. D. Axe, and G. Shirane, *Phys. Rev. B* **5** (1972), 1933. <https://doi.org/10.1103/PhysRevB.5.1933>
 - 26 J. F. Scott, *Rev. Mod. Phys.* **46** (1974), 83. <https://doi.org/10.1103/revmodphys.46.83>
 - 27 P. M. Woodward, *Acta Cryst.: Sect. B* **53** (1997), 44. <https://doi.org/10.1107/S0108768196012050>
 - 28 Y. Fujii, and S. Hoshino, *Phys. Rev. B* **9** (1974), 4549. <https://doi.org/10.1103/PhysRevB.9.4549>
 - 29 Ph. Ghosez, and K. M. Rabe. *Phys. Rev. B* **60** (1999), 836. <https://doi.org/10.1103/PhysRevB.60.836>
 - 30 D. Wang, J. Hlinka, A.A. Bokov, Z.-G. Ye, P. Ondrejovic, J. Petzelt, and L. Bellaiche, *Nat. Commun.* **5** (2014), 5100. <https://doi.org/10.1038/ncomms6100>
 - 31 Z. Jiang, B. Xu, F. Li, D. Wang, and C.-L. Jia, *Phys. Rev. B* **91** (2015), 014105. <https://doi.org/10.1103/PhysRevB.91.014105>
 - 32 D. S. Sholl and J. A. Steckel, (2010), *Density Functional Theory: A Practical Introduction*. (Wiley, 2009). <https://doi.org/10.1002/9780470447710>
 - 33 W. Zhong, D. Vanderbilt, and K. M. Rabe, *Phys. Rev. Lett.* **73** (1994), 1861. <https://doi.org/10.1103/PhysRevLett.73.1861>
 - 34 W. Zhong, D. Vanderbilt, and K. M. Rabe. *Phys. Rev. B* **52** (1995), 6301. <https://doi.org/10.1103/PhysRevB.52.6301>
 - 35 K. M. Rabe, and U. V. Waghmare, *Ferroelectrics* **164** (1995), 15. <https://doi.org/10.1080/00150199508221827>
 - 36 W. Zhong, and D. Vanderbilt, *Phys. Rev. Lett.* **74** (1995), 2587. <https://doi.org/10.1103/PhysRevLett.74.2587>
 - 37 A. M. Glazer, *Acta Cryst.: Sect. B* **28** (1972), 3384. <https://doi.org/10.1107/S0567740872007976>
 - 38 A. M. Glazer, *Acta Cryst.: Sect. A* **31** (1975), 756. <https://doi.org/10.1107/S0567739475001635>
 - 39 P. M. Woodward, *Acta Cryst. B* **53** (1997), 32. <https://doi.org/10.1107/S0108768196010713>
 - 40 R. J. Angel, J. Zhao, and N. L. Ross, *Phys. Rev. Lett.* **95** (2005), 025503. <https://doi.org/10.1103/PhysRevLett.95.025503>
 - 41 C. J. Howard, and H. T. Stokes, *Acta Cryst.: Sect. B* **54** (1998), 782. <https://doi.org/10.1107/S010876810200890X>
 - 42 H. T. Stokes, E. H. Kisi, D. M. Hatch, and C. J. Howard, *Acta Cryst.: Sect. B* **58** (2002), 934. <https://doi.org/10.1107/S0108768102015756>
 - 43 C. N. W. Darlington, *Acta Cryst.: Sect. A* **58** (2002), 299. <https://doi.org/10.1107/S0108767301016579>
 - 44 C. J. Howard, and H. T. Stokes, *Acta Cryst.: Sect. A* **61** (2005), 93. <https://doi.org/10.1107/S0108767304024493>
 - 45 K. F. Garrity, *Phys. Rev. B* **97** (2018), 024115. <https://doi.org/10.1103/PhysRevB.97.024115>
 - 46 A. Jain, G. Hautier, C. J. Moore, S. P. Ong, C. C. Fischer, T. Mueller, K. A. Persson, and G. Ceder, *Comput. Mater. Sci.* **50** (2011), 2295. <https://doi.org/10.1016/j.commatsci.2011.02.023>
 - 47 S. Curtarolo, W. Setyawan, S. Wang, J. Xue, K. Yang, R. H. Taylor, L. J. Nelson, G. L. Hart, S. Sanvito, M. Buongiorno Nardelli et al., *Comput. Mater. Sci.* **58** (2012), 227. <https://doi.org/10.1016/j.commatsci.2012.02.002>
 - 48 A. H. Larsen, J.J. Mortensen, J. Blomqvist, I.E. Castelli, R. Christensen, M. Dulak, J. Friis, M.N. Groves, B. Hammer, C. Hargus, E.D. Hermes, P.C. Jennings, P.B. Jensen, J. Kermode, J.R. Kitchin, E.L. Kolsbjerg, J. Kubal, K. Kaasbjerg, S. Lysgaard, J.B. Maronsson, T. Maxson, T. Olsen, L. Pastewka, A. Peterson, C. Rostgaard, J. Schiøtz, O. Schütt, M. Strange, K.S. Thygesen, T. Vegge, L. Vilhelmsen, M. Walter, Z. Zeng, and K.W. Jacobsen, *The atomic simulation environment—a Python library for working with atoms*, *J. Phys.: Condens. Matter* **29**, 273002 (2017). <https://doi.org/10.1088/1361-648X/aa680e>
 - 49 C. Michel, J. M. Moreau, G. D. Achenbach, R. Gerson, and W. J. James, *Solid State Commun.* **7** (1969). [https://doi.org/701.10.1016/0038-1098\(69\)90597-3](https://doi.org/701.10.1016/0038-1098(69)90597-3).
 - 50 Y. Chu, M. Cruz, C. Yang, L. Martin, P. Yang, J. Zhang, K. Lee, P. Yu, L. Chen, and R. Ramesh, *Adv. Mater.* **19** (2007), 2662. <https://doi.org/10.1002/adma.20060297231>
 - 51 S. H. Baek, H. W. Jang, C. M. Folkman, Y. L. Li, B. Winchester, J. X. Zhang, Q. He, Y. H. Chu, C. T. Nelson, M. S. Rzechowski, X. Q. Pan, R. Ramesh, L. Q. Chen, and C. B. Eom, *Nat. Mater.* **9** (2010), 309. <https://doi.org/10.1038/nmat2703>
 - 52 Z. Chen, Z. Chen, C.-Y. Kuo, L. W. Martin, et al. *Nat. Commun.* **9** (2018), 3764. <https://doi.org/10.1038/s41467-018-06190-5>
 - 53 I. Chung, J.-H. Song, J. Im, J. Androulakis, C. D. Malliakas, H. Li, A. J. Freeman, J. T. Kenney, and M. G. Kanatzidis, *J. Am. Chem. Soc.* **134** (2012), 8579. <https://doi.org/10.1021/ja301539s>
 - 54 M. Liu, M. B. Johnston, and H. J. Snaith, *Nature* **501** (2013), 395. <https://doi.org/10.1038/nature12509>
 - 55 L.-y. Huang, and W. R. L. Lambrecht, *Phys. Rev. B* **88** (2013), 165203. <http://doi.org/10.1103/PhysRevB.88.165203>
 - 56 E. L. Da Silva, J. M. Skelton, S. C. Parker, and A. Walsh, *Phys. Rev. B* **91** (2015), 144107. <http://doi.org/10.1103/PhysRevB.91.144107>
 - 57 J. P. Perdew, K. Burke, and M. Ernzerhof, *Phys. Rev. Lett.* **77** (1996), 3865. <https://doi.org/10.1103/PhysRevLett.77.3865>
 - 58 P. E. Blöchl, *Phys. Rev. B* **50** (1994), 17953. <https://doi.org/10.1103/PhysRevB.50.17953>
 - 59 J. Enkovaara, C. Rostgaard, J. J. Mortensen, et al. *J. Phys.: Condens. Matter* **22** (2010), 253202. <https://doi.org/10.1088/0953-8984/22/25/253202>
 - 60 The program is at <https://gitlab.com/pyseries/pytilting> and the documentation is at <https://dwang5.github.io/PyTiltingDoc/>.
 - 61 R. E. Cohen, and H. Krakauer, *Phys. Rev. B* **42** (1990), 6416. <https://doi.org/10.1103/PhysRevB.42.6416>
 - 62 R. E. Cohen, *Nature* **358** (1992), 136. <https://doi.org/10.1038/358136a0>
 - 63 H. J. Monkhorst, and J. D. Pack, *Phys. Rev. B* **13** (1976), 5188. <https://doi.org/10.1103/PhysRevB.13.5188>
 - 64 K. Momma, and F. Izumi, *J. Appl. Cryst.* **44** (2011), 1272. <https://doi.org/10.1107/S0021889811038970>
 - 65 A. Togo, L. Chaput, and I. Tanaka, *Phys. Rev. B* **91** (2015), 094306. <https://doi.org/10.1103/PhysRevB.91.094306>
 - 66 K. Leinenweber, and J. Parise, *J. Solid State Chem.* **114** (1995),

277. <https://doi.org/10.1006/jssc.1995.1040>
- ⁶⁷ L.-y. Huang, and W. R. L. Lambrecht, *Phys. Rev. B* **90** (2014), 195201. <https://doi.org/10.1103/PhysRevB.90.195201>
- ⁶⁸ N. A. Benedek, and C. J. Fennie, *J. Phys. Chem. C* **117** (2013), 13339. <https://doi.org/10.1021/jp402046t>
- ⁶⁹ R. D. Shannon, *Acta Cryst.: Sect. A* **32** (1976), 751. <https://doi.org/10.1107/S056773947600155>